A&A 679, A46 (2023)
https://doi.org/10.1051/0004-6361/202346710

Astronomy & Astrophysics

Searching for temporary gamma-ray dark blazars associated with IceCube neutrinos

E. Kun[1,2,3,4,5], I. Bartos[6], J. Becker Tjus[1,3], P. L. Biermann[7,8], A. Franckowiak[2], F. Halzen[9], and Gy. Mező[4,5]

[1] Theoretical Physics IV: Plasma-Astroparticle Physics, Faculty for Physics & Astronomy, Ruhr University Bochum, 44780 Bochum, Germany
[2] Faculty for Physics & Astronomy, Astronomical Institute, Ruhr University Bochum, 44780 Bochum, Germany
[3] Ruhr Astroparticle And Plasma Physics Center (RAPP Center), Ruhr-Universität Bochum, 44780 Bochum, Germany
[4] Konkoly Observatory, ELKH Research Centre for Astronomy and Earth Sciences, Konkoly Thege Miklós út 15-17, 1121 Budapest, Hungary
e-mail: kun@titan.physx.u-szeged.hu
[5] CSFK, MTA Centre of Excellence, Konkoly Thege Miklós út 15-17, 1121 Budapest, Hungary
[6] Department of Physics, University of Florida, PO Box 118440, Gainesville, FL 32611-8440, USA
[7] MPI for Radioastronomy, 53121 Bonn, Germany
[8] Department of Physics & Astronomy, University of Alabama, Tuscaloosa, AL 35487, USA
[9] Dept. of Physics, University of Wisconsin, Madison, WI 53706, USA

Received 20 April 2023 / Accepted 19 August 2023

ABSTRACT

Context. Tensions between the diffuse gamma-ray sky observed by the *Fermi* Large Area Telescope (*Fermi*-LAT) and the diffuse, high-energy neutrino sky detected by the IceCube South Pole Neutrino Observatory raise questions about our knowledge of high-energy neutrino sources in the gamma-ray regime. While blazars are among the most energetic persistent particle accelerators in the Universe, studies suggest that they could account for up to 10–30% of the neutrino flux measured by IceCube.
Aims. Our recent results highlight that the associated IceCube neutrinos arrived in a local gamma-ray minimum (dip) of three strong neutrino point-source candidates. Here, we increase the sample of neutrino-source candidates in order to study their gamma-ray light curves.
Methods. We generated the one-year *Fermi*-LAT light curve for eight neutrino-source candidate blazars (RBS 0958, GB6 J1040+0617, PKS 1313-333, TXS 0506+056, PKS 1454-354, NVSS J042025-374443, PKS 0426-380, and PKS 1502+106), centered on the detection time of the associated IceCube neutrinos. We applied the Bayesian block algorithm to the light curves to characterize their variability.
Results. Our results indicate that GB6 J1040+0617 was in a phase of high gamma-ray activity, while none of the other seven neutrino-source candidates were statistically bright during the detection of the corresponding neutrinos; indeed, most of the time neutrinos arrived in a faint gamma-ray phase of the light curves. This suggests either that the eight source candidate blazars (associated with seven neutrino events) in our reduced sample are not the sources of the corresponding IceCube neutrinos, or that an in-source effect (e.g., the suppression of gamma rays due to high gamma-gamma opacity) complicates the multimessenger scenario of neutrino emission for these blazars.

Key words. galaxies: active – gamma rays: galaxies – neutrinos – radio continuum: galaxies

1. Introduction

According to observations to date, the energetics of diffuse gamma rays (Ackermann et al. 2015), neutrinos (IceCube Collaboration 2021), and cosmic rays (Fenu & Pierre Auger Collaboration 2017) share similar power-law energetics. At lower energies, though, there is more flux in neutrinos than could be expected from gamma rays, if they are produced by the same sources. Results suggest that there could be a population of neutrino sources being obscured in gamma rays (e.g., IceCube Collaboration 2021). The tension at lower energies ($E < 100$ TeV) between the diffuse gamma-ray background measured by the *Fermi* Large Area Telescope (*Fermi*-LAT) and the diffuse neutrino background measured by the IceCube Neutrino Observatory also suggests the existence of a population of gamma-ray dark neutrino sources (Murase et al. 2016; Murase 2019), for which rather an anti-correlation holds between the neutrino and gamma-ray fluxes, at least in the epochs of efficient neutrino emission.

After a significant 3σ connection was found between a ∼290 TeV IceCube neutrino alert (IC-170922A) and the gamma-ray flaring blazar TXS 0506+056, this blazar quickly came into the focus of multimessenger astronomy. Follow-up searches in the offline IceCube data revealed a neutrino flare from the direction of TXS 0506+056 at the turn of the year 2014–2015 with an even higher significance (3.5σ). The individual events of this neutrino flare contained energies one order of magnitude lower (∼10 TeV) than the 2017 event, and they do not satisfy the strict selection cuts for single high-energy alerts.

As it turned out, the 2014–2015 neutrino flare (IceCube Collaboration 2018) happened during a low gamma-state of the source candidate blazar TXS 0506+056 (Garrappa et al. 2019a). An explanation suggests that if the medium is ideal for generating neutrinos it will absorb the pionic

gamma photons that are also generated in the hadronic process (Halzen et al. 2019; Halzen & Kheirandish 2020). Observations suggest this might actually be true, at least for a population of high-energy (HE) neutrino sources (e.g., Kun et al. 2021). The PeV–neutrino event called Big Bird arrived in the local minimum of a ∼85-day-long dip of the source candidate blazar PKS B1424-418 (Kadler et al. 2016). The neutrino event IC-190730A was detected from the direction of PKS 1502+106 when this blazar was in the middle of a deep, about 180-day-long gamma-ray minimum (Kun et al. 2021). The neutrino event IC-170922A was observed in a ∼28-day-long gamma-ray dip of TXS 0506+056.

As is discussed in Kun et al. (2021), temporal gamma-suppression potentially resolves the apparent contradiction of the blazar models simultaneously producing a detectable neutrino flux and a gamma flare, since at the time of efficient neutrino production the observed gamma photon flux drops, because the energy of pionic gamma rays cascades down to X-ray energies.

In this paper we examine eight *Fermi*-LAT blazars with good photon statistics (Kun et al. 2022) that we found within the 90% containment area of the 70 IceCube track-type neutrino events. In Sect. 2 we introduce our previous search to find neutrino-source candidates in the *Fermi*-LAT 4FGL-DR2 catalog, and summarize the source properties of individual neutrino-source candidates. In Sect. 3 we present our *Fermi*-LAT light curve analysis. In Sect. 4 we present our results, while in Sect. 5 we discuss them and give our conclusions.

2. Source selection

2.1. Previous catalog search to find Fermi-LAT 4FGL-DR2 neutrino-source candidates

In Kun et al. (2022), we searched gamma-ray, X-ray, and radio point sources in the 90% containment area of the 70 IceCube track-type neutrino events recorded between October 13, 2009 and September 30, 2019 and listed by Giommi et al. (2020). We found 29 gamma-ray neutrino-source candidates in the *Fermi*-LAT 4FGL-DR2 catalog (Abdollahi et al. 2020), 61 such X-ray point sources in the *Swift*-XRT Point Source catalog (keeping only the AGN-type objects, Evans et al. 2020), and 87(96) neutrino counterparts in the Combined Radio All-Sky Targeted Eight GHz Survey (Healey et al. 2007) at 4.8 GHz (8.4 GHz). These are the so-called ν-samples.

After the construction of the ν-samples, we conducted a randomness test of them to see if our selection method chooses random ν-samples or ν-samples with flux properties that are significantly different from the full catalogs. We note that we did not scramble the declinations of the neutrinos because of the strong variation in the sensitivity of IceCube with declination. We found that the constructed ν-samples represent special samples of sources taken from the full *Fermi*-LAT 4FGL-DR2/*Swift*-XRT 2SXPS/CRATES catalogs with similar significance (2.1σ, 1.2σ, 2σ at 4.8 GHz and 2.1σ at 8.4 GHz, respectively). In this sense, special means that the neutrinos do not randomly select samples. We already analyzed the neutrino-radio connection in Kun et al. (2022). After collecting redshifts and deriving subsamples of the CRATES catalog complete in the redshift–luminosity plane, we found that the 4.8 GHz (8.4 GHz) subsample can explain (90% C.L.) between 4% and 53% (3% and 42%) of the 70 IceCube track-type neutrino events listed by Giommi et al. (2020).

In this paper we focus on the possible neutrino-gamma ray connection. We list the name, the sky coordinates, the flux properties, the class, and the association of the 29 neutrino-source candidate *Fermi*-LAT blazars in Table 1. We generated the gamma-ray light curves plus and minus half a year around the detection time of the associated neutrinos. For sources with integrated flux below 10^{-9} ph cm^{-2} s^{-1} in the energy range from 0.1 to 100 GeV, and not experiencing bright flaring activity in the time window, there are not enough photon statistics to obtain good resolution on the light curve. We therefore applied the above gamma-ray photon flux threshold to obtain a sample of eight candidate sources (associated with seven neutrino events) from this selection that we study in the following. In the next subsection we introduce the eight neutrino-source candidate *Fermi*-LAT blazars that constitute our sample of interest in this study.

2.2. Individual neutrino-source candidates

RBS 0958 is a BL Lac object at redshift $z = 0.13793 \pm 0.00004$ (Ahn et al. 2012), associated with the *Fermi*-LAT source 4FGL J1117.0+2013. RBS 0958 is a high-synchrotron peaked (e.g., Paiano et al. 2017) VHE candidate (Furniss et al. 2015) and is considered to be a candidate TeV emitter based on the position of its synchrotron peak (Costamante et al. 2018). RBS 0958 was observed by the High Energy Stereoscopic System (H.E.S.S.) as having an integral flux upper limit of $I(>610\,\mathrm{GeV}) = 1.44 \times 10^{-12}$ ph cm^{-2} s^{-1} (Aharonian 2015).

GB6 J1040+0617 is a low-synchrotron peaked BL Lac object at redshift $z = 0.7351 \pm 0.0045$ (Ahn et al. 2012; Maselli et al. 2015), associated with the *Fermi*-LAT source 4FGL J1040.5+0617. Garrappa et al. (2019a) highlights the increased gamma-ray activity of this source for a period of ∼90 days around the time of the neutrino detection. Gabányi et al. (2019) analyzed 3.4 μm and 4.6 μm band GB6 J1040+0617 data of the Wide-field Infrared Survey Explorer (*WISE*). They find the source was brightest, increasing its flux density by almost 90%, in the mission phase preceding the neutrino event IceCube-141209A by 4.5 days.

PKS 1313-333 is a flat-spectrum radio quasar (FSRQ) at redshift $z \approx 1.210$ (Jauncey et al. 1982), associated with the *Fermi*-LAT source 4FGL J1316.1-3338. *Fermi*-LAT detected an increasing gamma-ray flux from a source positionally consistent with PKS 1313-333[1], which was confirmed by Astro-rivelatore Gamma a Immagini Leggero (AGILE)[2]. Integrating photons from 02:00 UT on January 10, 2016 to 02:00 UT on January 12, 2016, a maximum likelihood analysis of AGILE data yields the detection of the source at a significance level of about 5σ, with a flux of $(1.6 \pm 0.6) \times 10^{-6}$ ph cm^{-2} s^{-1} ($E > 100$ MeV), in agreement with the *Fermi*-LAT measurement. An increasing gamma-ray flux was observed again in 2021[3].

TXS 0506+056 is a BL Lac object (suggested to have at least temporarily intrinsic properties of a FSRQ, Padovani et al. 2019) at redshift $z = 0.3365 \pm 0.0010$ (Paiano et al. 2018), associated with the *Fermi*-LAT source 4FGL J0509.4+0542. This source is a TeV[4] emitter. A multimessenger campaign, triggered by the coincident observation of a gamma-ray flare and the 290 TeV IceCube neutrino IC-170922A (assuming a neutrino spectrum of $\varepsilon_\nu^{-2.19}$), identified TXS 0506+056 as the possible source of high-energy neutrinos at a 3σ significance level (IceCube Collaboration et al. 2018). With this, TXS 0506+056

[1] https://www.astronomerstelegram.org/?read=8533
[2] https://www.astronomerstelegram.org/?read=8536
[3] https://www.astronomerstelegram.org/?read=14672
[4] http://tevcat.uchicago.edu/?mode=1&showsrc=309

Table 1. Source properties of the 29 neutrino-source candidates from the 10-year *Fermi*-LAT point–source catalog (4FGL-DR2), published in Kun et al. (2022).

4FGL ID	RA (°)	Dec (°)	$N_{\rm pred}$	F_{1000} (ph cm^{-2} s^{-1})	$F_{\rm peak}$ (ph cm^{-2} s^{-1})	Class	Association
(1)	(2)	(3)	(4)	(5)	(6)	(7)	(8)
4FGL J2030.5+2235	307.64	22.59	117.0	1.36e−10	–	–	–
4FGL J2030.9+1935	307.74	19.60	526.8	8.24e−10	–	BLL	RX J2030.8+1935
4FGL J1808.2+3500	272.07	35.01	730.8	3.72e−10	1.75e−08	BLL	MG2 J180813+3501
4FGL J1808.8+3522	272.22	35.38	305.6	1.91e−10	–	BLL	2MASX J18084968+3520426
4FGL J1744.2-0353	266.05	−3.89	740.6	3.90e−10	–	FSRQ	PKS 1741-03
4FGL J0230.3+1713	37.60	17.22	537.5	2.52e−10	–	–	–
4FGL J0224.9+1843	36.23	18.72	983.7	1.70e−10	4.52e−08	FSRQ	TXS 0222+185
4FGL J1117.0+2013	169.27	20.23	1442.3	**1.25e−09**	2.09e−08	BLL	RBS 0958
4FGL J2227.9+0036	336.98	0.62	679.9	8.70e−10	–	BLL	PMN J2227+0037
4FGL J1233.0+1333	188.26	13.56	828.0	3.34e−10	–	–	–
4FGL J1040.5+0617	160.15	6.28	2927.1	**1.49e−09**	6.26e−08	BLL	GB6 J1040+0617
4FGL J0854.0+2753	133.52	27.88	28.4	3.93e−11	–	BLL	SDSS J085410.16+275421.7
4FGL J1557.9-0001	239.49	−0.02	412.3	1.86e−10	–	FSRQ	PKS 1555+001
4FGL J1258.7-0452	194.68	−4.87	124.1	1.73e−10	–	BLL	RBS 1194
4FGL J1311.8+2057	197.97	20.96	617.2	5.30e−11	–	BCU	MG2 J131144+2052
4FGL J0103.5+1526	15.88	15.43	294.7	1.74e−10	–	BLL	TXS 0100+151
4FGL J1316.1-3338	199.03	−33.64	3866.4	**2.39e−09**	1.22e−07	FSRQ	PKS 1313-333
4FGL J0244.7+1316	41.19	13.28	574.5	2.01e−10	1.78e−08	Blazar	GB6 J0244+1320
4FGL J1447.0-2657	221.77	−26.96	195.1	1.64e−10	–	BCU	NVSS J144657-265713
4FGL J1439.5-2525	219.88	−25.42	153.9	1.55e−10	–	BCU	NVSS J143934-252458
4FGL J0509.4+0542	77.36	5.70	7619.8	**8.02e−09**	1.94e−07	BLL	TXS 0506+056
4FGL J1457.4-3539	224.37	−35.65	5233.2	**3.49e−09**	2.56e−07	FSRQ	PKS 1454-354
4FGL J1505.0-3433	226.26	−34.55	642.8	3.77e−10	2.15e−08	BLL	PMN J1505-3432
4FGL J2351.4-2818	357.87	−28.31	290.7	1.28e−10	–	–	–
4FGL J0420.3-3745	65.09	−37.75	1841.0	**1.09e−09**	3.43e−08	BCU	NVSS J042025-374443
4FGL J0428.6-3756	67.17	−37.94	24240.3	**2.36e−08**	3.57e−07	BLL	PKS 0426-380
4FGL J1504.4+1029	226.10	10.50	25352.5	**2.02e−08**	9.72e−07	FSRQ	PKS 1502+106
4FGL J0946.2+0104	146.57	1.07	201.8	2.15e−10	–	BLL	1RXS J094620.5+010459
4FGL J0948.9+0022	147.24	0.37	7769.2	**2.29e−09**	1.61e−07	NLSY1	PMN J0948+0022 $^{(\star)}$

Notes. The columns are: (1) 4FGL source ID, (2) right-ascension (J2000, in degrees), (3) declination (J2000, in degrees), (4) predicted number of photons, (5) photon flux between 0.1–100 GeV, (6) peak photon flux, (7) class: BLL=BL Lac class of blazar, FSRQ=FSRQ class of blazar, BCU=active galaxy of uncertain class, (8) association name. Sources with F_{1000} values above 10^{-9} ph cm^{-2} s^{-1} are marked by boldface. $^{(\star)}$: this source is within 1.5 times the 90% containment area of the respective neutrino and was included in error in Kun et al. (2022).

became the first identified source of high-energy cosmic neutrinos at such a high significance. The blazar TXS 0506+056 is 0.1° away from the best-fit neutrino location of IC-170922A (56.5% signalness). The quantity signalness is the probability that an observed neutrino has an astrophysical ($s = 1$) or atmospheric ($s = 0$) origin (see its definition in Aartsen et al. 2017). Going back to the archival data, the IceCube Collaboration found a 160-day-long neutrino flare in 2014–2015 from the direction of TXS 0506+056 at a significance level of 3.5σ (IceCube Collaboration 2018). Despite being more dominant than IC-170922A, this neutrino flare happened during a low-gamma state of TXS 0506+056 (Garrappa et al. 2019a). Putting this behavior into a common physical picture with IC-170922A and the coincident gamma-flare still challenges the current blazar models.

The Major Atmospheric Gamma Imaging Cherenkov Telescopes (MAGIC) measured the upper limit on the >90 GeV flux of TXS 0506+056 as $<3.56 \times 10^{-11}$ ph cm^{-2} s^{-1} in the epoch MJD 58020.18 (Ansoldi et al. 2018), about 1 day after the detection of IC-170922A, and MAGIC measured a significant increase in >90 GeV flux, $(4.7 \pm 1.4) \times 10^{-11}$ ph cm^{-2} s^{-1} at MJD 58029.22, and $(8.7 \pm 2.0) \times 10^{-11}$ ph cm^{-2} s^{-1} at MJD 58030.24, 10–11 days after the detection of IC-170922A. Confirming this elevated high-energy state, the Very Energetic Radiation Imaging Telescope Array System (VERITAS) Collaboration reported the integral flux (>110 GeV) of TXS 0506+056 as $(8.9 \pm 1.6) \times 10^{-12}$ ph cm^{-2} s^{-1} (Abeysekara et al. 2018). H.E.S.S. performed follow-up observations of the high-energy neutrino on September 23, 2017 and the following night (September 24, 2017 at 03:10 UTC). A preliminary on-site calibration and analysis searching for a point-like gamma-ray source from within the 90% uncertainty region of the neutrino event IC-170922A revealed no significant detection (upper limit $<1.0 \times 10^{-11}$ ph cm^{-2} s^{-1} for >175 GeV, Schüssler et al. 2019). Employing the ANTARES neutrino telescope data recorded in a cone of 3°, centered on the best-fit coordinates of IC-170922A and within a ±1 h time-window centered on the event time, Albert et al. (2018) constrained the neutrino fluence to <15 GeV cm^{-2} for $\gamma = 2$ (integrated between 3.3 TeV and 3.4 PeV) and to <34 GeV cm^{-2} for $\gamma = 2.5$ (integrated between 450 GeV and 280 TeV), assuming a point source with power-law spectrum $\mathrm{d}N/\mathrm{d}E \sim E^{-\gamma}$.

The radio flux density of TXS 0506+056 measured by the Owens Valley 40m Radio telescope started to increase in the

beginning of 2016, and was still increasing after the neutrino detection. During the 2014–2015 neutrino flare, the radio flux density was average. With very long baseline interferometry (VLBI), the radio jet of TXS 0506+056 shows strong signs of spine-sheath structure within the inner 1 mas, corresponding to about 70–140 pc in the deprojected distance from the millimeter-VLBI core (Ros et al. 2020). It has been shown that at 15 GHz (e.g., Kun et al. 2019) and 43 GHz (Ros et al. 2020) the VLBI core is responsible for the radio brightening. Several scenarios have been suggested to explain the neutrino emission (Britzen et al. 2019; Garrappa et al. 2019a; Reimer et al. 2019; Petropoulou et al. 2020; Zhang et al. 2020).

PKS 1454-354 is a low-synchrotron peaked FSRQ type blazar at redshift $z \approx 1.424$ (Jackson et al. 2002), associated with the *Fermi*-LAT source 4FGL J1457.4-3539. This source is located within the 90% error ellipse of the neutrino IC-181014A. The *Fermi*-LAT collaboration reported an increase in gamma-ray activity from the source in September 2008 (Abdo et al. 2009). PKS 1454-354 has a weak one-sided jet.

NVSS J042025-374443 is a radio source at the (photometric) redshift $z \approx 0.3$ (Malkin 2018), associated with the *Fermi*-LAT source 4FGL J0420.3-3745. This is another >100 MeV gamma-ray source located within the 90% IC-190504A localization error, at a distance of roughly 37 arcmin from the best-fit neutrino localization (PKS 0426-380 is located at a distance of roughly 72 arcmin).

PKS 0426-380 is a reclassified FSRQ at redshift $z \approx 1.111$ (Heidt et al. 2004; Sbarufatti et al. 2005), associated with the *Fermi*-LAT source 4FGL J0428.6-3756. This source is located within the 90% error ellipse of the neutrino IC-190504A. Tanaka et al. (2013) reported the *Fermi*-LAT detection of two very-high-energy ($E \sim 100$ GeV) gamma-ray photons from the directional vicinity of PKS 0426-380. Zhang et al. (2017) find a possible gamma-ray quasi-periodicity of this blazar with a period of 3.35 ± 0.68 yr at the significance level of approximately 3.6σ.

PKS 1502+106 is an FSRQ, the fifteenth brightest gamma-ray source at >100 MeV in terms of energy flux among 2,863 sources in the fourth catalog of AGN detected by *Fermi*-LAT (4LAC Ajello et al. 2020). The redshift of PKS 1502+106 was estimated to be $z = 1.839$ (Smith et al. 1977), later confirmed by the good signal-to-noise ratio spectrum of the Sloan Digital Sky Survey (SDSS; $z = 1.8385 \pm 0.0024$ at high confidence, Schneider et al. 2010). Given its distance and still-enormous observed gamma-ray photon flux, PKS 1502+106 must have extremely high intrinsic luminosity. This source is highly variable in the *Fermi*-LAT gamma-ray band (Abdo et al. 2010a). It showed strong gamma-ray flares in the *Fermi*-LAT energy range in 2008 (Abdo et al. 2010b). The flaring activity of PKS 1502+106 was renewed between 2009 and 2010. From 2015, the source showed more strong gamma-ray flares (see e.g., in Kun et al. 2021).

VLBI observations reveal a one-sided, curved radio jet and a bright core structure at parsec scales (e.g., Karamanavis et al. 2016). At radio frequencies, the source is also highly variable.

The IceCube detector recorded a high-energy neutrino event on June 30, 2019 (with 67% signalness) that was distributed through the Gold alert stream (IceCube Collaboration 2019). The most probable neutrino energy was approximately 300 TeV, assuming a $\varepsilon_\nu^{-2.19}$ neutrino spectrum. PKS 1502+106 lies with an offset of 0.31° from the best-fit neutrino location of IC-190730A. At the time of the corresponding neutrino detection, PKS 1502+106 was in a quiet state in the optical (Stein et al. 2019; Lipunov et al. 2019), UV (Franckowiak et al. 2020), X-ray (Santander et al. 2019; Kun et al. 2021), and gamma-ray regimes (Garrappa et al. 2019b). A long-term radio outburst that started in 2014 had just reached its peak flux when the IceCube neutrino was recorded (Kiehlmann et al. 2019). This source became part of the Icecube and ANTARES a priori defined monitored source list (34 gamma-ray bright AGN).

After the detection of IC-190730A, the nearby candidate PKS 1502+106 quickly became the center of focus of many studies. Kun et al. (2021) studied cosmic neutrinos from temporarily gamma-suppressed blazars, such as PKS 1502+106. As it is shown, the neutrino event IC-190730A (IceCube Collaboration 2019) arrived during an exceptionally low gamma-ray state of PKS 1502+106 that lasted for several months. Rodrigues et al. (2021) identify one quiescent state and two flaring states with hard and soft gamma-ray spectra. They find two hadronic models that can describe the multiwavelength emission during all three states: a leptohadronic model with a contribution from photohadronic processes to X-rays and gamma rays, and a proton synchrotron model where the emission from keV to 10 GeV comes from proton synchrotron radiation. Oikonomou et al. (2021) analyzed UV, optical, and X-ray observations of PKS 1502+106, as well as collecting other multiwavelength data. They find that the leptohadronic modeling, in which the multiwavelength emission of PKS 1502+106 originates beyond the broad-line region (BLR) and inside the dust torus, is most consistent with the observations. Analyzing 15 GHz Very Long Baseline Array (VLBA) and astrometric 8 GHz VLBA data, Britzen et al. (2021) present evidence for a radio ring structure that develops with time. They suggest that the neutrino IC-190730A was most likely produced by proton-proton interaction in the blazar zone beyond the BLR, enabled by episodic encounters of the jet with dense clouds, that is to say some molecular clouds in the narrow line region.

3. Analysis of *Fermi*-LAT data of eight blazars

The LAT instrument on board the *Fermi* Gamma-ray Space Telescope is designed to cover the energy band from 20 MeV to greater than 300 GeV. In this study we employed one year of Pass8 *Fermi*-LAT[5] data[6] for each of the eight *Fermi*-LAT neutrino-source candidates, in a time range plus and minus half a year centered on the detection time of the corresponding neutrinos listed in Table 2. The region of interest (ROI) was centered at the J2000 sky coordinates of the 4FGL-DR2 sources, encompassing an area of the sky within 15° ROI radius. We selected event type "front+back" (evtype=3), which is the recommended type for a point source analysis.

We generated the likelihood light curve of the eight brightest 4FGL-DR2 neutrino-source candidates. We performed a binned likelihood analysis of the data utilizing the fermipy v1.0.1 and ScienceTools v2.0.8 packages, both built in the FermiBottle Docker container and analysis environment provided by the *Fermi* Science Support Center[7]. The analysis was carried out on a cluster of 16 vCPU-s (Intel Skylake 16 × 2.2 GHz) in the ELKH Cloud[8]. The instrument

[5] https://fermi.gsfc.nasa.gov/science/instruments/lat.html
[6] https://fermi.gsfc.nasa.gov/ssc/data/analysis/documentation/Pass8_usage.html
[7] https://github.com/fermi-lat/FermiBottle
[8] https://science-cloud.hu/

Table 2. Source properties of neutrino-source candidates from 4FGL-DR2 that were considerably bright during our one-year observational window ($F_{1000} > 10^{-9}$ ph cm^{-2} s^{-1}, see with boldface in Table 1).

Source	4FGL ID	RA (°)	Dec (°)	Class	z	ID$_\nu$	RA$_\nu$ (°)	Dec$_\nu$ (°)	$T_{\mathrm{MJD},\gamma}$ (days)
(1)	(2)	(3)	(4)	(5)	(6)	(7)	(8)	(9)	(10)
RBS 0958	J1117.0+2013	169.27	20.23	BLL	0.1379	IC-130408A	$168.16^{+2.87}_{-1.9}$	$20.67^{+1.15}_{-0.89}$	[56207.6–56572.8]
GB6 J1040+0617	J1040.5+0617	160.15	6.28	BLL	0.7351	IC-141209A	$159.81^{+0.84}_{-1.04}$	$6.57^{+0.64}_{-0.56}$	[56817.5–57182.8]
PKS 1313-333	J1316.1-3338	199.03	−33.64	FSRQ	1.210	IC-160814A	$199.39^{+2.43}_{-3.03}$	$-32.4^{+1.39}_{-1.21}$	[57432.3–57797.5]
TXS 0506+056	J0509.4+0542	77.36	5.70	BLL	0.3365	IC-170922A	$77.43^{+0.95}_{-0.65}$	$5.72^{+0.5}_{-0.3}$	[57836.2–58201.5]
PKS 1454-354	J1457.4-3539	224.37	−35.65	FSRQ	1.424	IC-181014A	$224.3^{+1.4}_{-2.85}$	$-34.8^{+1.15}_{-1.85}$	[58222.9–58588.1]
NVSS J042025-374443	J0420.3-3745	65.09	−37.75	BCU	0.300	IC-190504A	$65.79^{+1.23}_{-1.23}$	$-37.44^{+1.23}_{-1.23}$	[58425.1–58790.4]
PKS 0426-380	J0428.6-3756	67.17	−37.94	FSRQ	1.111	IC-190504A	$65.79^{+1.23}_{-1.23}$	$-37.44^{+1.23}_{-1.23}$	[58425.1–58790.4]
PKS 1502+106	J1504.4+1029	226.10	10.50	FSRQ	1.839	IC-190730A	$225.52^{+1.28}_{-1.43}$	$10.47^{+1.14}_{-0.89}$	[58512.2–58877.5]

Notes. The columns are: (1) source name, (2) 4FGL source ID, (3) right-ascension (J2000, in degrees), (4) declination (J2000, in degrees), (5) type, (6) redshift, (7) neutrino ID (8), neutrino right-ascension (J2000), (9) neutrino declination (J2000), (10) time window for *Fermi*-LAT analysis.

response functions `P8R3_SOURCE_V2` were employed together with templates of the Galactic interstellar emission model `gll_iem_v07.fits` and of the isotropic diffuse emission `iso_P8R3_SOURCE_V2_v1.txt`[9]. We applied the nominal data quality cut `(DATA_QUAL > 0) && (LAT_CONFIG==1)`, and a zenith angle cut $\theta < 90°$ to eliminate Earth limb events. Time intervals when the Sun was closer than 15° to the target sources were filtered out.

The detection level of each source was measured by the definition of test statistic (TS, Mattox et al. 1996), and the detection limit of new sources was set to $TS_{\mathrm{min}} = 25$ ($\sim 5\sigma$). The test statistic is defined as $TS = -2\ln(L_{\mathrm{max},1}/L_{\mathrm{max},0})$, where $L_{\mathrm{max},0}$ is the maximum likelihood value for a model without an additional source (the "null hypothesis") and $L_{\mathrm{max},1}$ is the maximum likelihood value for a model with the additional source at a specified location.

Since the two models are nested, according to Wilks' theorem (Wilks 1938) the TS-distribution will asymptotically follow a χ^2 distribution. Then the TS distribution should be drawn from a $\chi^2{}_n$ distribution, where n is the difference in the degree of freedom between the models with and without the additional source. In our *Fermi*-LAT analysis the normalization factor of the Galactic and isotropic diffuse components and sources with $TS > 25$ were freed. We associated power-law profiles to the additional sources that are detected in our analysis but that do not appear in the 4FGL-DR2. We consider new point sources to be separate sources if the angular distance between them is larger then 0.3 degrees. We present a summary of additional sources found in the ROI of seven target sources in Table A.1. To get more information about variability in the light curves, we applied the adaptive binning algorithm (Lott et al. 2012), setting the relative flux uncertainty to 15%. With adaptive binning, our analysis is more sensitive to the light variations. To achieve the same photon statistics throughout the light curve, the bins are shorter when the source is bright and the bins are wider when the source is fainter.

We repeated the analysis with 3–4 days fixed binning for two sources that have the best photon statistics in our sample, namely TXS 0506+056 and PKS 1502+106. We show the light curve for these sources with fixed binning overplotted on their adaptively binned light curve in Appendix C (see Figs. C.1 and C.2, respectively). The shapes of the light curves with fixed binning are similar to the adaptively binned light curves, but with fixed binning the light curves are more noisy when the sources were faint. In comparing the results from the two light curve generation methods, we do not see different structures that would alter the results of this paper. Moreover, fixed binning of the light curve of the other sources in our sample, being fainter than the two shown here, would lead to a large amount of non-detections. This further justifies the choice of the adaptive binning method employed in our work.

[9] `https://fermi.gsfc.nasa.gov/ssc/data/access/lat/BackgroundModels.html`

4. Results

Below, we refer to the centers and widths of the bins in the form of center ±width/2 in order to help understand the time characteristics of the bins. We note here that the ± does not mean an error. We modeled the light curves of the neutrino-source candidates between 100 MeV and 300 GeV, except for GB6 J1040+0617, PKS 1313-333, and TXS 0506+056, where, to avoid contamination by the neighboring bright gamma-ray sources, we set the minimum energy of the analysis to 300 MeV. We fit the normalization factor and the spectral index of the source of interest in each bin. Normalization of sources with TS-value > 25 and sources within 5 degrees of the source of interest was also free (regardless of their test statistic). To better understand significant variations in the light curves, we applied the Bayesian block algorithm of Scargle et al. (2013) to them. Following Garrappa et al. (2019a), we set the probability to $p = 0.05$. The Bayesian blocks are shown on the light curve of the gamma-ray sources in the appendix, as stated below, from source to source. We summarize the characteristic timing and flux values of minimum and maximum photon flux bins compared to the neutrino bins in Table 3, and elaborate more on the results below.

RBS 0958 is located 1.19° away from the best-fit localization of the neutrino event IC-130408A, within the 90% error ellipse of the neutrino. We show the one-year-long likelihood light curve of RBS 0958 in Fig. B.1 along with the photon index as function of time. The corresponding neutrino was detected in T_ν = MJD 56390.1887627, with reconstructed neutrino energy of $E_\nu = 30.8^{+3.3}_{-3.5}$ TeV. The neutrino came in the *Fermi*-LAT bin MJD 56417.0 ± 29.4 days, with an average flux of $(1.46 \pm 0.58) \times 10^{-8}$ ph cm^{-2} s^{-1}. This bin is situated on the decreasing branch of a gamma flare, which is centered to MJD 56303.2 ± 10.0 days (86.97 days before the neutrino detection). Though the Bayesian blocks (with $p = 0.05$) do not indicate a significantly variable flux during the one-year-long time window (see Fig. B.1), the peak photon flux of the suspected flare ($(8.0 \pm 2.4) \times 10^{-8}$ ph cm^{-2} s^{-1}) is about 45–83 times higher

Table 3. Characteristic timing and flux values of the minimum and maximum gamma-ray flux bins compared to the neutrino bins, and the p-values of the gamma-ray photon flux of the neutrino bin being the maximum flux in the light curve.

Source	N	$t_{F\nu}$	F_ν	$t_{F\min} - t_{F\nu}$	$F_{\min}/F_\nu$	$t_{F\max} - t_{F\nu}$	$F_{\max}/F_\nu$	p
(–)	(–)	(MJD)	(ph cm^{-2} s^{-1})	(days)	(–)	(days)	(–)	(–)
(1)	(2)	(3)	(4)	(5)	(6)	(7)	(8)	(9)
RBS 0958	8	56417.0	$(1.46 \pm 0.58) \times 10^{-8}$	123.2	0.57 ± 0.34	−113.8	5.46 ± 2.70	0.519
GB6 J1040+0617	8	56994.9	$(1.57 \pm 0.46) \times 10^{-8}$	−86.1	0.01 ± 0.26	0.0	1.00 ± 0.41	0.133
PKS 1313-333	5	57632.6	$(5.94 \pm 2.44) \times 10^{-9}$	102.1	0.39 ± 0.37	−61.0	4.36 ± 2.34	0.701
TXS 0506+056	76	58018.0	$(1.10 \pm 0.32) \times 10^{-7}$	−155.2	0.20 ± 0.11	−80.1	2.94 ± 0.99	0.386
PKS 1454-354	4	58396.7	$(2.73 \pm 1.80) \times 10^{-8}$	−98.30	0.04 ± 0.14	169.03	3.00 ± 2.19	0.372
NVSS J042025-374443	3	58575.1	$(9.50 \pm 4.93) \times 10^{-9}$	135.0	0.78 ± 0.58	−105.0	1.43 ± 0.92	0.539
PKS 0426-380	49	58607.8	$(1.97 \pm 0.41) \times 10^{-7}$	−143.6	0.07 ± 0.06	43.5	1.91 ± 0.65	0.219
PKS 1502+106	50	58703.2	$(5.40 \pm 1.01) \times 10^{-8}$	0.00	1.00 ± 0.26	−112.3	6.31 ± 1.91	0.935

Notes. The columns are: (1) source name, (2) number of gamma-ray bins of the light curve of the source (N), (3) MJD of the neutrino bin ($t_{F\nu}$), (4) average photon flux of the neutrino bin (F_ν), (5) MJD of the minimum flux bin ($t_{F\min}$) minus MJD of the neutrino bin ($t_{F\nu}$), (6) average flux of the minimum flux bin ($F_{\min}$) over the flux of the neutrino bin (F_ν), (7) MJD of the maximum flux bin ($t_{F\max}$) minus MJD of the neutrino bin ($t_{F\nu}$), (8) average flux of the maximum flux bin ($F_{\max}$) over the flux of the neutrino bin (F_ν), and (9) p-value (p).

than the average photon flux of RBS 0958 in the 4FGL-DR2 catalog (1.24×10^{-9} ph cm^{-2} s^{-1}). This indicates that there might indeed be a gamma-ray flare going on in this window. Based on its photon indices, RBS 0958 shows signs of spectral softening during the gamma-ray flare. The peak flux of this flare was $(7.97 \pm 2.35) \times 10^{-8}$ ph cm^{-2} s^{-1}, which is about 5.5 times the flux of the bin in the gamma-ray light curve containing the detected neutrino (from here on we refer to this specific bin of the gamma-ray light curve as "neutrino bin"). The bins before (MJD 56370.6 ± 17.0) and after (MJD 56477.0 ± 30.6) the neutrino bin have similar fluxes to the flux of the neutrino bin ($(1.65 \pm 1.02) \times 10^{-8}$ ph cm^{-2} s^{-1} and $(1.08 \pm 0.59) \times 10^{-8}$ ph cm^{-2} s^{-1}, respectively).

GB6 J1040+0617 is located within the 90% error ellipse of IC-141209A, 0.45° away from the best-fit localization of the neutrino. We show the one-year-long likelihood light curve of GB6 J1040+0617 in Fig. B.2 along with the photon index as a function of time. The corresponding neutrino was detected in T_ν = MJD 57000.14311, with reconstructed neutrino energy of $E_\nu = 97.4^{+9.6}_{-9.6}$ TeV. The neutrino came in the *Fermi*-LAT bin MJD 56994.9 ± 22.8 days, with an average flux of $(1.57 \pm 0.46) \times 10^{-8}$ ph cm^{-2} s^{-1}. This is the peak flux of the gamma-ray flare shown by this source during the one-year-long light curve centered on the time of the neutrino detection. The flux in the previous bin (MJD 56949.6 ± 22.5) is about half the flux of the neutrino bin ($(7.9 \pm 4.1) \times 10^{-9}$ ph cm^{-2} s^{-1}). The flux in the next bin (MJD 57038.2 ± 20.5) is about 2/3 of the flux in the neutrino bin ($(1.11 \pm 0.38) \times 10^{-8}$ ph cm^{-2} s^{-1}).

PKS 1313-333 is located within the 90% error ellipse of IC-160814A (T_ν = MJD 57614.91), 1.29° away from its best-fit sky coordinates. We show the one-year-long likelihood light curve of PKS 1313-333 in Fig. B.3 along with the photon index as a function of time. The neutrino came in the *Fermi*-LAT bin MJD 57632.6 ± 51.0, with flux of $(5.9 \pm 2.4) \times 10^{-9}$ ph cm^{-2} s^{-1}. The previous bin, which is the peak of the light curve, is situated at MJD 57571.6 ± 10.0 with a flux of $(2.57 \pm 0.91) \times 10^{-8}$ ph cm^{-2} s^{-1}, which is more than four times the flux of the neutrino bin. The next bin (MJD 57734.7 ± 51.0) has an average flux of $(2.3 \pm 2.0) \times 10^{-9}$ ph cm^{-2} s^{-1}, about half the flux of the neutrino bin. This is also the faintest bin of the light curve.

TXS 0506+056 is located within the 90% error ellipse of IC-170922A (T_ν = MJD 58018.87), 0.1° away from its best-fit sky coordinates. We show the one-year-long likelihood light curve of TXS 0506+056 in Fig. B.4 along with the photon index as a function of time. The neutrino came in the 2.3-day-long *Fermi*-LAT bin centered to MJD 58018.0, which has a flux of $(1.10 \pm 0.32) \times 10^{-7}$ ph cm^{-2} s^{-1}. This bin is on the decreasing side of a gamma-ray dip. The highest-flux bin (MJD 57938.0 ± 0.8) has a flux of $(3.23 \pm 0.64) \times 10^{-7}$ ph cm^{-2} s^{-1}, which is about three times the flux in the neutrino bin. The highest-flux bin is situated 80.0 days before the detection time of the neutrino. The minimum flux of the light curve $(2.2 \pm 0.1) \times 10^{-8}$ ph cm^{-2} s^{-1} is reached in the bin MJD 57962.8 ± 3.3, centered 155 days prior to the detection.

PKS 1454-354 is located within the 90% error ellipse of IC-181014A (T_ν = MJD 58405.5), 0.85° away from best-fit sky coordinates of this neutrino event. We show the one-year-long likelihood light curve of PKS 1454-354 in Fig. B.5 along with the photon index as a function of time. The neutrino came in the *Fermi*-LAT bin MJD 58396.7 ± 22.8, with the photon flux of $(2.7 \pm 1.8) \times 10^{-8}$ ph cm^{-2} s^{-1}, indicating the source was in a faint phase. We note that the photon flux in the neutrino bin is about an order of magnitude larger than the average photon flux of this source in the 4FGL-DR2 catalog (3.49×10^{-9} ph cm^{-2} s^{-1}), and that it is about an order of magnitude smaller than the peak photon flux of this source in the same catalog (2.56×10^{-7} ph cm^{-2} s^{-1}).

NVSS J042025-374443 is located within the 90% error ellipse of IC-190504A (T_ν = MJD 58607.77), 0.76° away from its best-fit sky coordinates. We show the one-year-long likelihood light curve of NVSS J042025-374443 in Fig. B.6 along with the photon index as a function of time. Though the source is rather faint in the studied observational window, permitting us to get only three bins of the light curve, we can note the following. The neutrino came in the *Fermi*-LAT bin MJD 58575.1 ± 60, with a flux of $(9.5 \pm 4.9) \times 10^{-9}$ ph cm^{-2} s^{-1}. The previous bin is situated as MJD 58470.1 ± 45.0, with a flux of $(1.36 \pm 0.52) \times 10^{-8}$ ph cm^{-2} s^{-1}. The next bin, MJD 58710.1 ± 75, has an average flux of $(7.4 \pm 3.9) \times 10^{-9}$ ph cm^{-2} s^{-1}. The highest-flux bin, MJD 58470.1 ± 45.0, is centered 137.63 days before the detection time of the corresponding neutrino and has an average flux of $(1.36 \pm 0.52) \times 10^{-8}$ ph cm^{-2} s^{-1}. We note that

the photon flux of the neutrino bin is 4–13 times higher than the average photon flux of this source in the 4FGL-DR2 catalog (1.09×10^{-9} ph cm^{-2} s^{-1}), and about 2–8 times smaller than the peak photon flux of the source in the 4FGL-DR2 catalog (3.56×10^{-8} ph cm^{-2} s^{-1}).

PKS 0426-380 is also located within the 90% error ellipse of IC-190504A (T_ν = MJD 58607.77), 1.47° away from its best-fit sky positions. We show the one-year-long likelihood light curve of PKS 0426-380 in Fig. B.7 along with the photon index as a function of time. The neutrino came in the *Fermi*-LAT bin MJD 58607.8 ± 2.7 that has an average flux of $(1.97 \pm 0.41) \times 10^{-7}$ ph cm^{-2} s^{-1}. The highest-flux gamma-ray bin MJD 58651.3 ± 1.6 is centered 43.6 days after the neutrino, and the peak of a gamma-ray flare shown by the source. This light curve bin has an average flux of $(3.76 \pm 1.02) \times 10^{-7}$ ph cm^{-2} s^{-1}, which is about two times higher than the flux of the neutrino bin. PKS 0426-380 is a significantly stronger gamma source than the other gamma source, NVSS J042025-374443, that also lies within the 90% error ellipse of IC-190504A.

PKS 1502+106 is located within the 90% error ellipse of IC-190730A (T_ν = MJD 58694.87), 0.58° away from the best-fit sky coordinates of the corresponding neutrino. This 299 TeV event was distributed through the Gold channel of the IceCube real-time alert system. Its signalness is 0.67 and the false alarm rate is 0.677 yr^{-1}. We show the one-year likelihood light curve of PKS 1502+106 in Fig. B.8 along with the photon index as a function of time. The neutrino came in the *Fermi*-LAT bin MJD 58703.2 ± 25.5, which has a flux of $(5.4 \pm 1.0) \times 10^{-8}$ ph cm^{-2} s^{-1}. This bin marks the global minimum of the one-year light curve of PKS 1502-106, the lowest-flux bin of a prolonged deep minimum lasting about 178 days. The highest-flux bin (MJD 58590.9 ± 7.0), centered 112 days before the neutrino detection, has an average flux of $(3.4 \pm 0.8) \times 10^{-7}$ ph cm^{-2} s^{-1}), which is more than six times the flux of the neutrino bin.

5. Discussion and conclusions

High-energy, low-optical-depth neutrino formation processes predict that the neutrino flux is proportional to the gamma-ray photon flux and one therefore expects the emission of high-energy neutrinos during gamma flares.

We calculated the chance probability of detecting a neutrino in a bin with a gamma-ray photon flux higher then the observed gamma-ray photon flux of the neutrino bin:

$$p = P(F_{\gamma,\max} > F_{\gamma,\nu}) = \frac{\Sigma_i \int_{F_{\gamma,\nu}}^{\infty} \mathcal{N}(x, F_i, \sigma_i) \mathrm{d}Fx}{\Sigma_i \int_{-\infty}^{\infty} \mathcal{N}(x, F_i, \sigma_i) \mathrm{d}Fx} \quad (1)$$

where $\mathcal{N}(x, F_i, \sigma_i)$ is the Gaussian evaluated at x, when we assume the uncertainty of the flux is normally distributed. When the p-value is close to zero, it means that the neutrino came in gamma maximum and there is no chance of getting higher gamma-ray photon flux during the studied time range. This is the case when the medium is transparent to the gamma photons and we see a gamma peak during the detection of high-energy neutrinos from the source.

When the p-value is close to unity, it means that the neutrino came in a gamma minimum and therefore all bins of the light curve are brighter than the flux of the bin in which the neutrino arrived. This is the case when the neutrino flux and gamma-ray photon flux are anti-correlated, for example due to the high in-source gamma-gamma optical depth, and at the time of maximum neutrino emissivity the pionic gamma photons are maximally absorbed and cascade down to X-ray energies. This is the case of beam dampening. Using the above considerations we calculated the p-values (see in Table 3).

It seems that the corresponding neutrino came in the global maximum of the one-year-long gamma light curve of GB6 J1040+0617, and in global minimum of the one-year long gamma light curve of PKS 1502+106. For the other neutrino-source candidates, PKS 1313-333, PKS 1454-354 NVSS J042025-374443, RBS 0958, TXS 0506+056, and PKS 0426-380, the neutrino arrival time seems to not correlate with the gamma-ray photon flux, even though fainter phases are more characteristic of the neutrino arrivals.

What we can conclude is that, apart from GB6 J1040+0617, none of the neutrino-source candidates were significantly bright in a time window of ±6 months around the corresponding IceCube neutrinos. We note here that our findings are based on a one-year-long gamma-ray photon flux curve of the respective sources. Taking into account the whole *Fermi*-LAT light curves might alter the outcomes of this analysis.

The fact that, out of the eight neutrino candidate sources (associated with seven neutrino events) studied, we find only one neutrino-source candidate blazar at peak gamma-ray photon flux during the neutrino emission means that either the sources in our sample are not the sources of the corresponding IceCube neutrinos, or an in-source effect (e.g., the suppression of gamma rays due to high gamma-gamma opacity, Kun et al. 2021) complicates the multimessenger scenario of neutrino emission, at least for these blazars. It is also possible that a mix of these two scenarios is at play. Future studies conducted at even higher energies, at which gamma-ray absorption should be more evident, or alternative measurements, such as HI column density measurements, might be helpful to disambiguate between these scenarios.

Acknowledgements. We thank Simone Garrappa, Deirdre Horan, Josefa Becerra Gonzalez, Melissa Pesce Rollins and Patrik Milán Veres for comments and discussions. We acknowledge support from the Deutsche Forschungsgemeinschaft DFG, within the Collaborative Research Center SFB1491 "Cosmic Interacting Matters – From Source to Signal" (project No. 445052434). E.K. thanks the Alexander von Humboldt Foundation for its Postdoctoral Fellowship. I.B. acknowledges the support of the Alfred P. Sloan Foundation and NSF grants PHY-1911796 and PHY-2110060. This paper makes use of publicly available *Fermi*-LAT data provided online by the https://fermi.gsfc.nasa.gov/ssc/data/access/ *Fermi* Science Support Center. On behalf of Project '*fermi*-agn' we thank for the usage of the ELKH Cloud that significantly helped us achieving the results published in this paper.

References

Aartsen, M. G., Ackermann, M., Adams, J., et al. 2017, Astropart. Phys., 92, 30
Abdo, A. A., Ackermann, M., Ajello, M., et al. 2009, ApJ, 699, 976
Abdo, A. A., Ackermann, M., Ajello, M., et al. 2010a, ApJS, 188, 405
Abdo, A. A., Ackermann, M., Ajello, M., et al. 2010b, ApJ, 710, 810
Abdollahi, S., Acero, F., Ackermann, M., et al. 2020, ApJS, 247, 33
Abeysekara, A. U., Archer, A., Benbow, W., et al. 2018, ApJ, 861, L20
Ackermann, M., Ajello, M., Albert, A., et al. 2015, ApJ, 799, 86
Aharonian, F. 2015, IAU Gener. Assem., 29, 2236508
Ahn, C. P., Alexandroff, R., Allende Prieto, C., et al. 2012, ApJS, 203, 21
Ajello, M., Angioni, R., Axelsson, M., et al. 2020, ApJ, 892, 105
Albert, A., André, M., Anghinolfi, M., et al. 2018, ApJ, 863, L30
Ansoldi, S., Antonelli, L. A., Arcaro, C., et al. 2018, ApJ, 863, L10
Britzen, S., Fendt, C., Böttcher, M., et al. 2019, A&A, 630, A103
Britzen, S., Zajaček, M., Popović, L. Č., et al. 2021, MNRAS, 503, 3145
Costamante, L., Cutini, S., Tosti, G., Antolini, E., & Tramacere, A. 2018, MNRAS, 477, 4749
Evans, P. A., Page, K. L., Osborne, J. P., et al. 2020, ApJS, 247, 54
Fenu, F., & Pierre Auger Collaboration 2017, in 35th International Cosmic Ray Conference (ICRC2017), 301, 486

Franckowiak, A., Garrappa, S., Paliya, V., et al. 2020, ApJ, 893, 162
Furniss, A., Sutter, P. M., Primack, J. R., & Domínguez, A. 2015, MNRAS, 446, 2267
Gabányi, K. É., Frey, S., & Moór, A. 2019, Res. Notes Am. Astron. Soc., 3, 36
Garrappa, S., Buson, S., Franckowiak, A., et al. 2019a, ApJ, 880, 103
Garrappa, S., Buson, S., Gasparrini, D., & Fermi-LAT Collaboration 2019b, GRB Coordinates Network, 25239, 1
Giommi, P., Glauch, T., Padovani, P., et al. 2020, MNRAS, 497, 865
Halzen, F., & Kheirandish, A. 2020, Nat. Phys., 16, 498
Halzen, F., Kheirandish, A., Weisgarber, T., & Wakely, S. P. 2019, ApJ, 874, L9
Healey, S. E., Romani, R. W., Taylor, G. B., et al. 2007, ApJS, 171, 61
Heidt, J., Tröller, M., Nilsson, K., et al. 2004, A&A, 418, 813
IceCube Collaboration 2018, Science, 361, 147
IceCube Collaboration 2019, GRB Coordinates Network, 25225, 1
IceCube Collaboration 2021, Phys. Rev. D, 104, 022002
IceCube Collaboration, Fermi-LAT, MAGIC, et al. 2018, Science, 361, 147
Jackson, C. A., Wall, J. V., Shaver, P. A., et al. 2002, A&A, 386, 97
Jauncey, D. L., Batty, M. J., Gulkis, S., & Savage, A. 1982, AJ, 87, 763
Kadler, M., Krauß, F., Mannheim, K., et al. 2016, Nat. Phys., 12, 807
Karamanavis, V., Fuhrmann, L., Krichbaum, T. P., et al. 2016, A&A, 586, A60
Kiehlmann, S., Hovatta, T., Kadler, M., Max-Moerbeck, W., & Readhead, A. C. S. 2019, ATel, 12996, 1
Kun, E., Biermann, P. L., & Gergely, L. Á. 2019, MNRAS, 483, L42
Kun, E., Bartos, I., Tjus, J. B., et al. 2021, ApJ, 911, L18
Kun, E., Bartos, I., Becker Tjus, J., et al. 2022, ApJ, 934, 180
Lipunov, V., Gorbovskoy, E., Kornilov, V., et al. 2019, ATel, 12971, 1
Lott, B., Escande, L., Larsson, S., & Ballet, J. 2012, A&A, 544, A6
Malkin, Z. 2018, ApJS, 239, 20
Maselli, A., Massaro, F., D'Abrusco, R., et al. 2015, Ap&SS, 357, 141
Mattox, J. R., Bertsch, D. L., Chiang, J., et al. 1996, ApJ, 461, 396
Murase, K. 2019, in 36th International Cosmic Ray Conference (ICRC2019), 36, 965
Murase, K., Guetta, D., & Ahlers, M. 2016, Phys. Rev. Lett., 116, 071101a
Oikonomou, F., Petropoulou, M., Murase, K., et al. 2021, JCAP, 2021, 082
Padovani, P., Oikonomou, F., Petropoulou, M., Giommi, P., & Resconi, E. 2019, MNRAS, 484, L104
Paiano, S., Franceschini, A., & Stamerra, A. 2017, MNRAS, 468, 4902
Paiano, S., Falomo, R., Treves, A., & Scarpa, R. 2018, ApJ, 854, L32
Petropoulou, M., Murase, K., Santander, M., et al. 2020, ApJ, 891, 115
Reimer, A., Böttcher, M., & Buson, S. 2019, ApJ, 881, 46
Rodrigues, X., Garrappa, S., Gao, S., et al. 2021, ApJ, 912, 54
Ros, E., Kadler, M., Perucho, M., et al. 2020, A&A, 633, L1
Santander, M., Keivani, A., & Tohuvavohu, A. 2019, ATel, 12985, 1
Sbarufatti, B., Treves, A., Falomo, R., et al. 2005, AJ, 129, 559
Scargle, J. D., Norris, J. P., Jackson, B., & Chiang, J. 2013, ApJ, 764, 167
Schneider, D. P., Richards, G. T., Hall, P. B., et al. 2010, AJ, 139, 2360
Schüssler, F., Ashkar, H., Backes, M., et al. 2019, in 36th International Cosmic Ray Conference (ICRC2019), 36, 787
Smith, H. E., Burbidge, E. M., Baldwin, J. A., et al. 1977, ApJ, 215, 427
Stein, R., Franckowiak, A., Kasliwal, M. M., et al. 2019, ATel, 12974, 1
Tanaka, Y. T., Cheung, C. C., Inoue, Y., et al. 2013, ApJ, 777, L18
Wilks, S. S. 1938, Ann. Math. Statist., 9, 60
Zhang, P.-F., Yan, D.-H., Liao, N.-H., et al. 2017, ApJ, 842, 10
Zhang, B. T., Petropoulou, M., Murase, K., & Oikonomou, F. 2020, ApJ, 889, 118

Appendix A: Additional sources found in the ROI of the target sources

Table A.1. Additional sources in the ROI about the target sources.

Source ID	RA	DEC	Δd	$F_{1000} \times 10^{10}$	err$F_{1000} \times 10^{10}$	TS	$N_{\rm pred}$
-	(°)	(°)	(°)	(ph cm^{-2} s^{-1})	(ph cm^{-2} s^{-1})	-	-
(1)	(2)	(3)	(4)	(5)	(6)	(7)	(8)
RBS 0958							
PS J1106.9+2708	166.719	27.139	7.29	2.39	1.13	18.38	154.21
PS J1132.6+2738	173.161	27.642	8.219	7.80	1.97	58.02	60.53
GB6 J1040+0617							
PS J1042.6+0838	160.655	8.637	2.405	7.89	1.72	441.27	615.38
PKS 1313-333							
PS J1242.8-2554	190.720	-25.912	10.557	5.07	1.70	8.1	32.42
PS J1246.4-2602	191.610	-26.039	9.950	8.68	0.12	60.65	123.66
TXS 0506+056							
PS J0500.7-0140	75.183	-1.671	7.686	22.32	0.18	365.95	383.90
NVSS J042025-374443							
PS J0347.8-3618	56.952	-36.316	6.654	4.62	1.25	40.84	147.55
PS J0348.7-3029	57.184	-30.484	9.774	3.06	1.01	131.58	424.67
PS J0454.4-3140	73.614	-31.667	9.271	2.44	1.09	20.71	133.68
PKS 0426-380							
PS J0456.4-4318	74.113	-43.302	7.511	3.80	1.31	53.98	370.24
PKS 1502+106							
PS J1446.6+1213	221.652	12.216	4.690	3.37	0.14	16.96	60.75
PS J1525.8+1636	231.470	16.605	8.030	4.14	0.33	48.66	350.34

Notes. Source ID (1), right-ascension J2000 (2), declination J2000 (3), offset of the new source to the target source (4), flux measured by Fermi between 0.1 GeV and 100 GeV (5), error of the flux value (6), TS-value of the detection (7), predicted number of photons (8).

Appendix B: Light curves

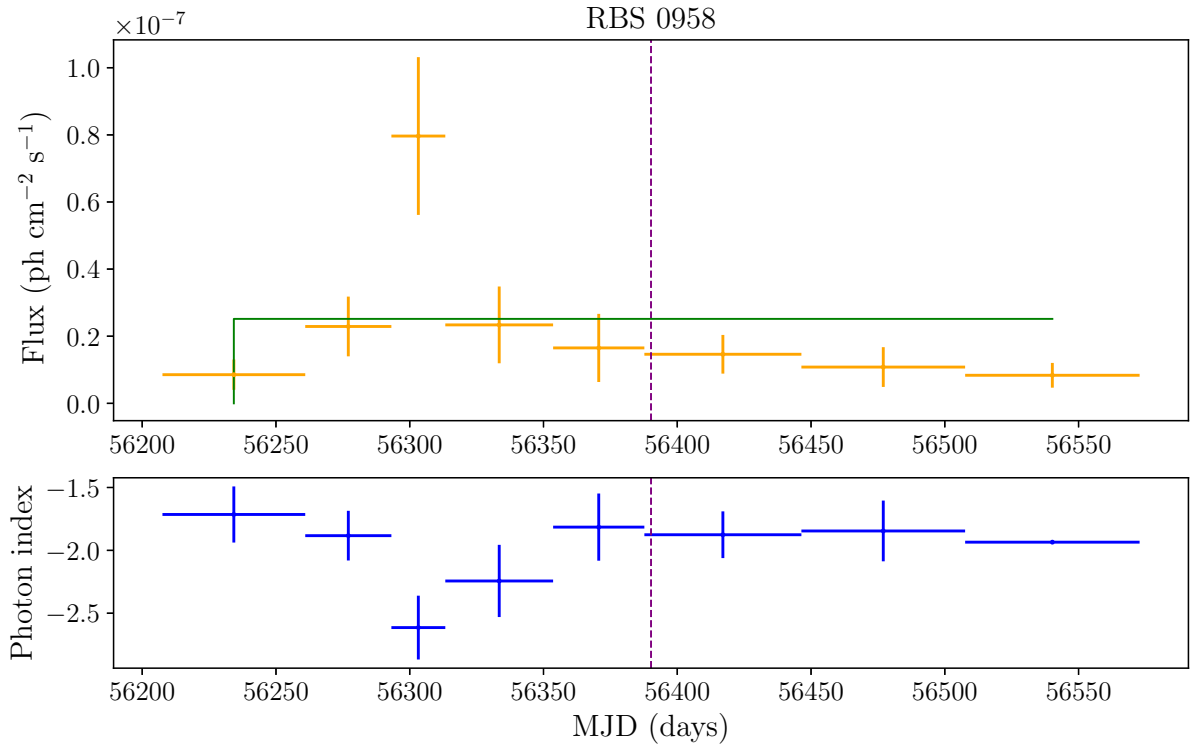

Fig. B.1. Gamma-ray flux variation of RBS 0958. Upper panel: likelihood light curve of RBS 0958 with Bayesian blocks ($p = 0.05$). The continuous green line represents the Bayesian block binning. Lower panel: photon index as a function of time.

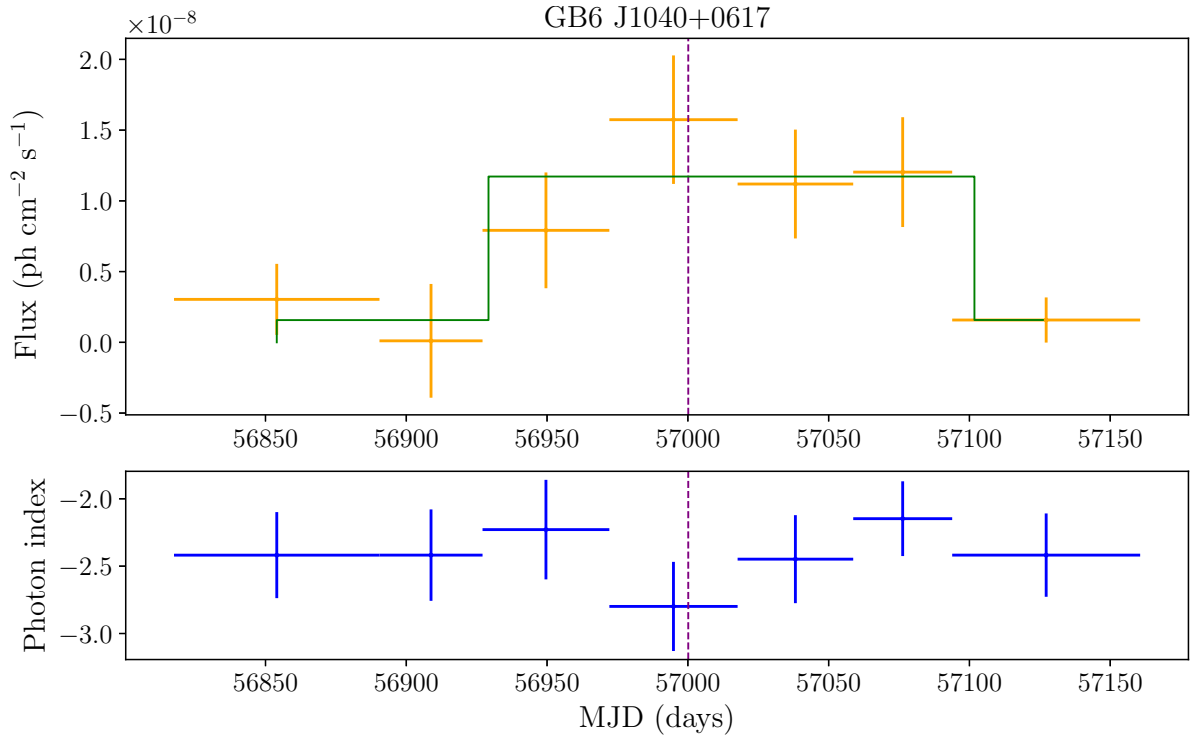

Fig. B.2. Gamma-ray flux variation of Upper panel: likelihood light curve with Bayesian blocks ($p = 0.05$). The continuous green line represents the Bayesian block binning. Lower panel: photon index as a function of time.

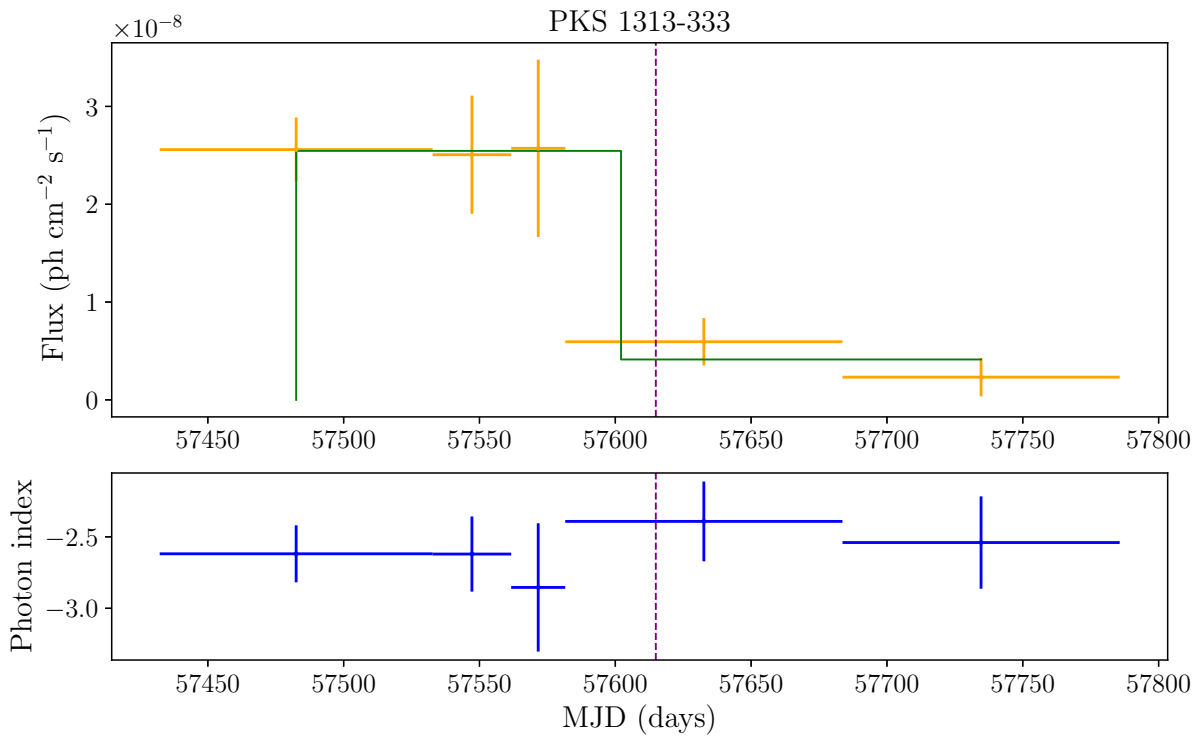

Fig. B.3. Gamma-ray flux variation of PKS 1313-333. Upper panel: likelihood light curve with Bayesian blocks ($p = 0.05$). The continuous green line represents the Bayesian block binning. Lower panel: photon index as a function of time.

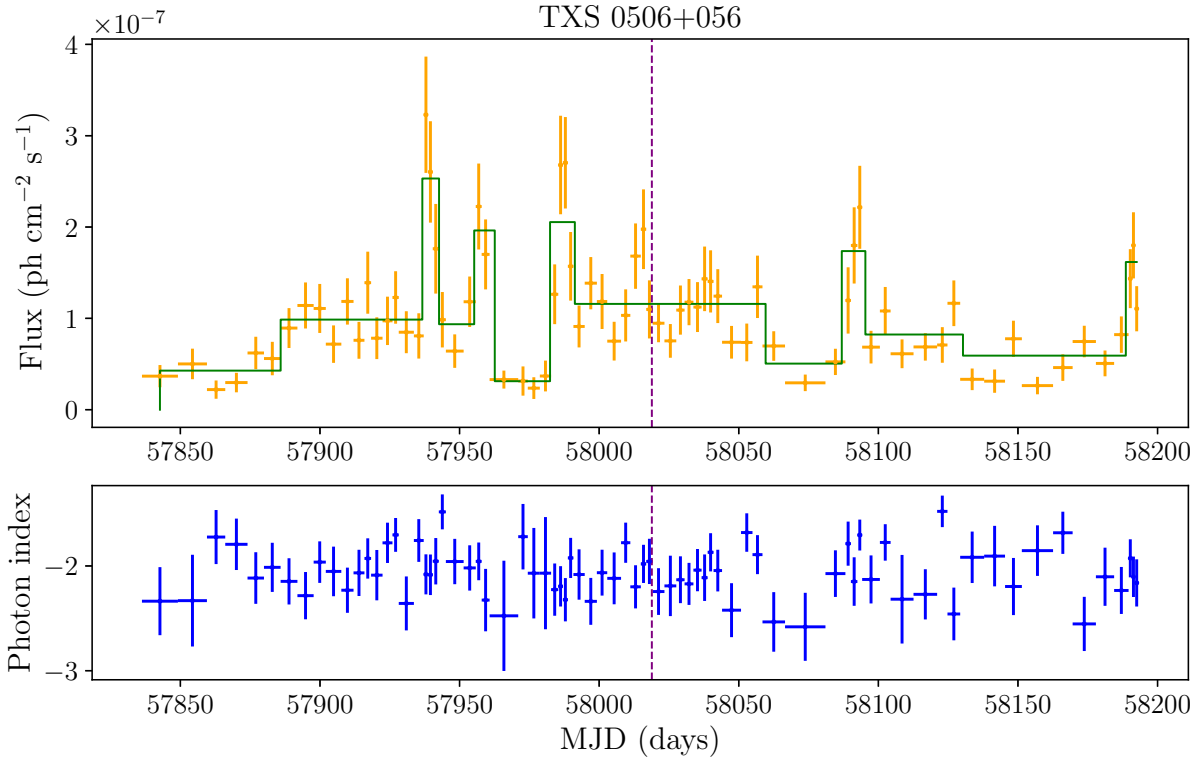

Fig. B.4. Gamma-ray flux variation of TXS 0506+056. Upper panel: likelihood light curve with Bayesian blocks ($p = 0.05$). The continuous green line represents the Bayesian block binning. Lower panel: photon index as a function of time.

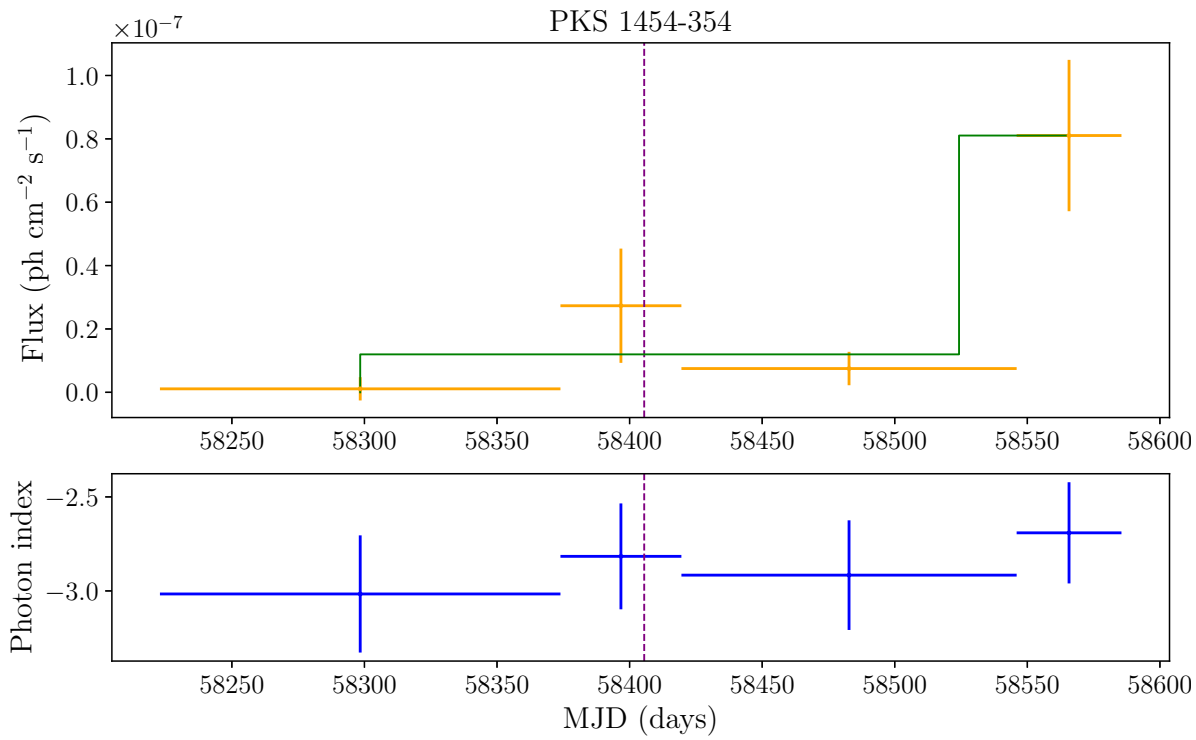

Fig. B.5. Gamma-ray flux variation of PKS 1454-354. Upper panel: likelihood light curve with Bayesian blocks ($p = 0.05$). The continuous green line represents the Bayesian block binning. Lower panel: photon index as a function of time.

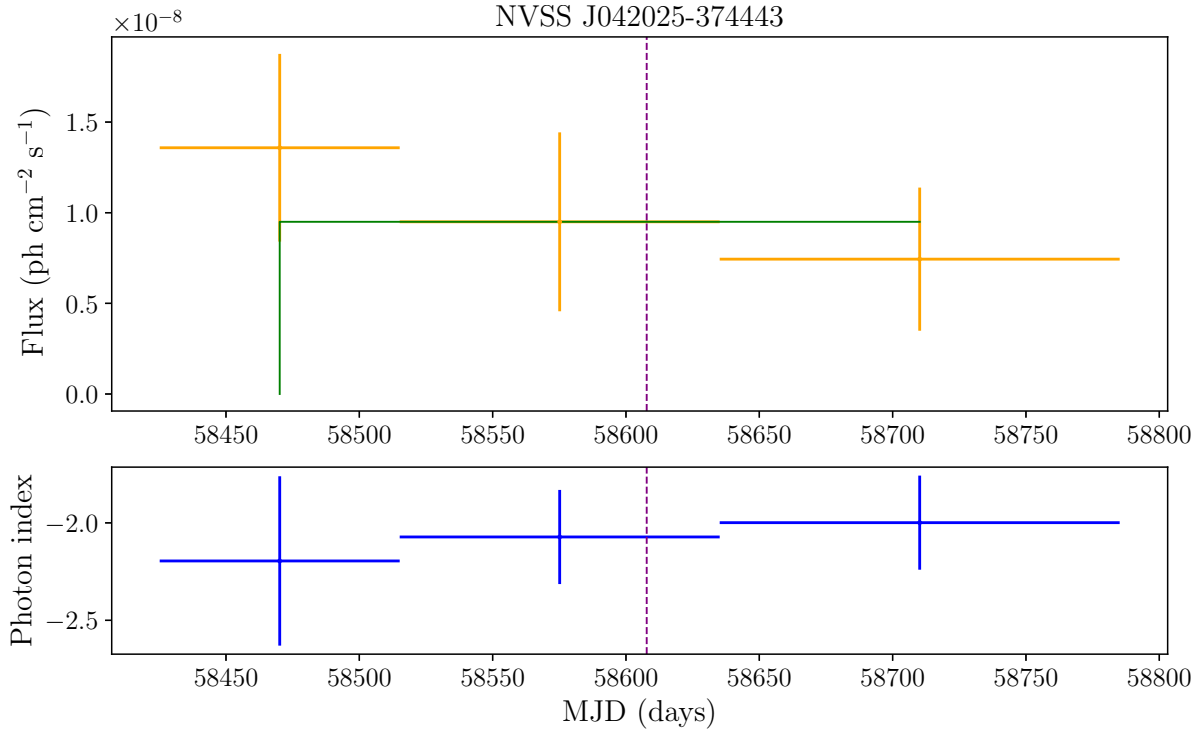

Fig. B.6. Gamma-ray flux variation of NVSS J042025-374443. Upper panel: likelihood light curve with Bayesian blocks ($p = 0.05$). The continuous green line represents the Bayesian block binning. Lower panel: photon index as a function of time.

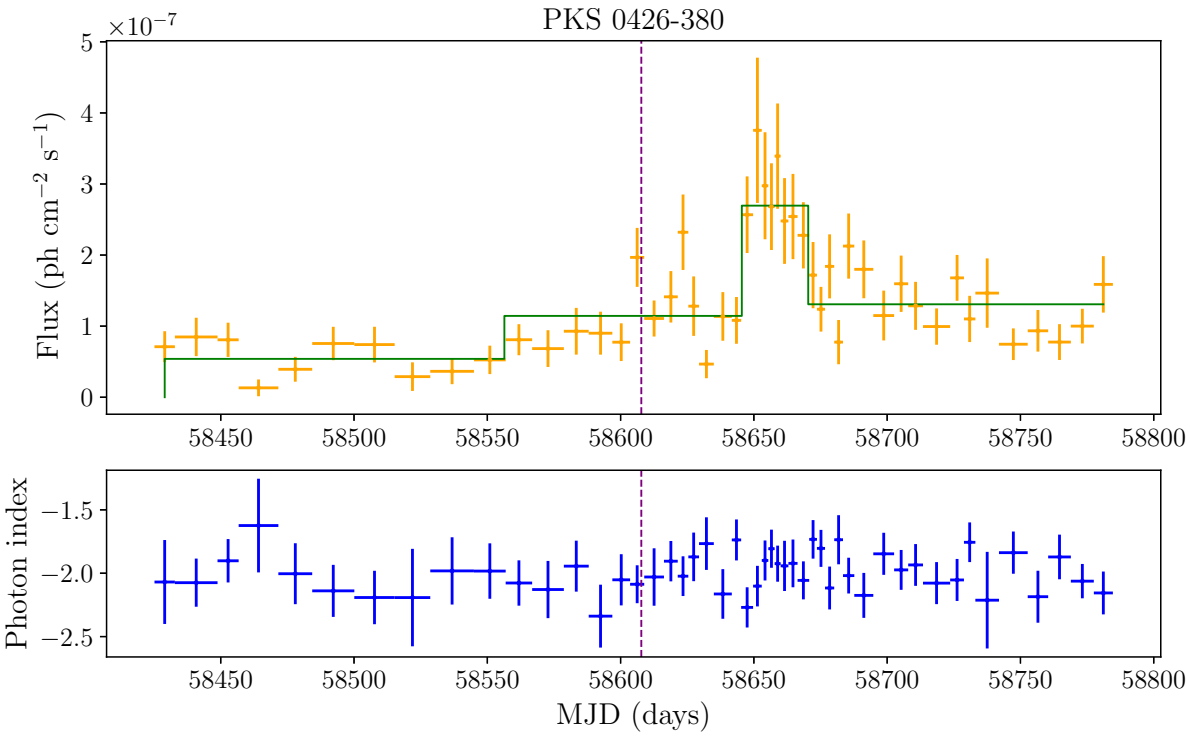

Fig. B.7. Gamma-ray flux variation of PKS 0426-380. Upper panel: likelihood light curve with Bayesian blocks ($p = 0.05$). The continuous green line represents the Bayesian block binning. Lower panel: photon index as a function of time.

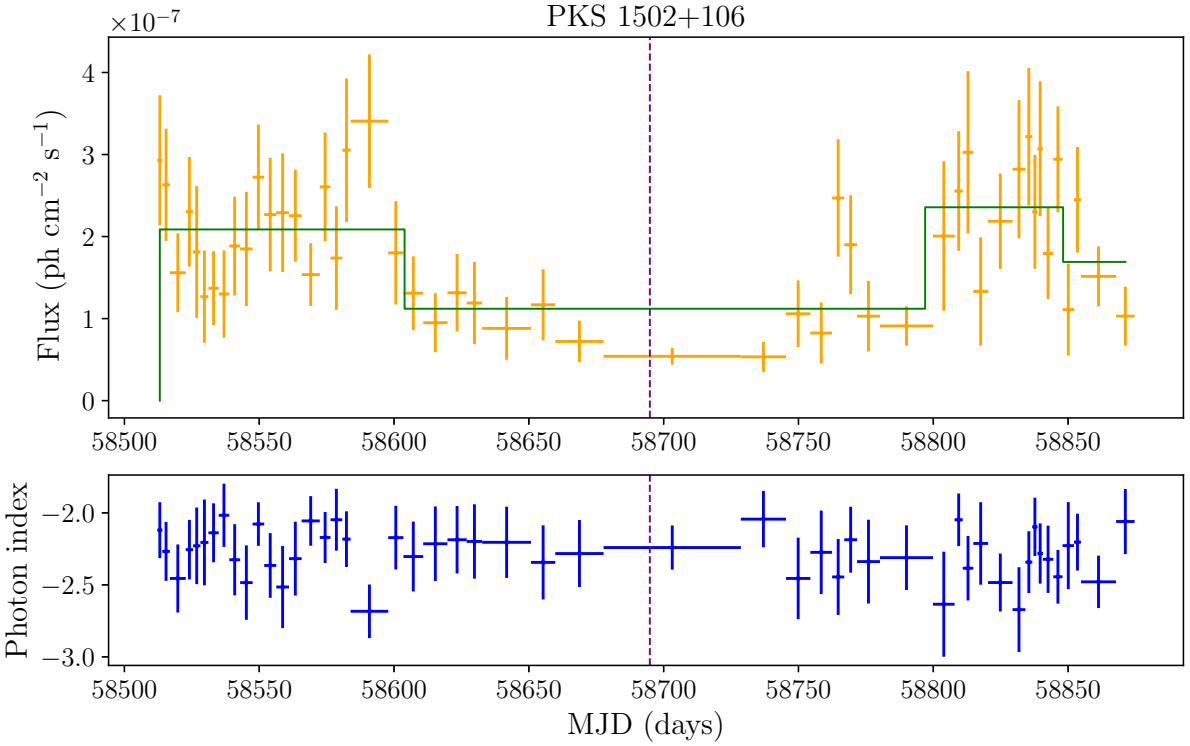

Fig. B.8. Gamma-ray flux variation of PKS 1502+106. Upper panel: likelihood light curve with Bayesian blocks ($p = 0.05$). The continuous green line represents the Bayesian block binning. Lower panel: photon index as function of time.

Appendix C: Comparison of adaptive and fixed binning of the light curves of two bright sources

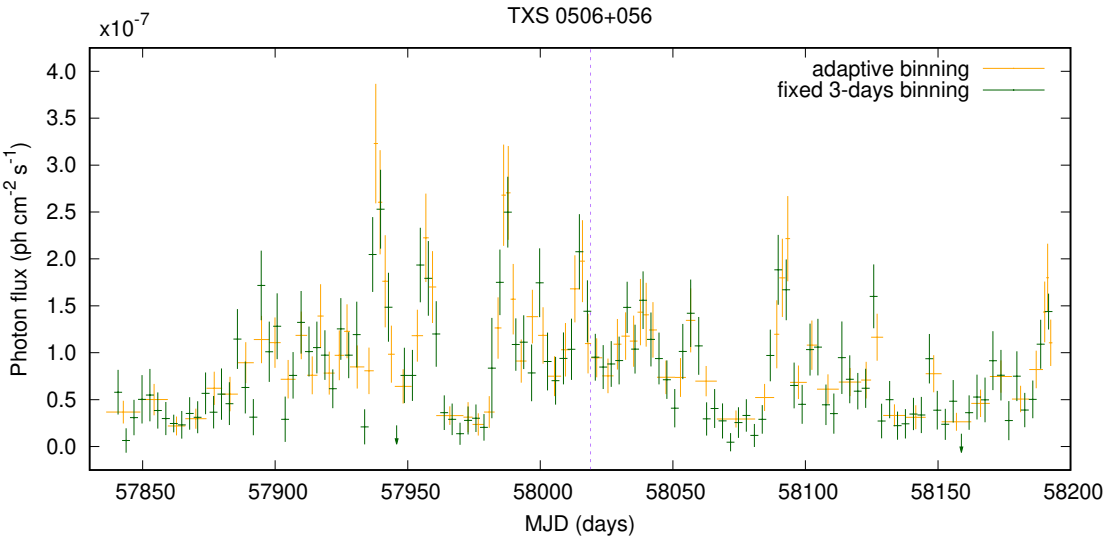

Fig. C.1. Light curve of TXS 0506+056 with fixed binning (green crosses) overplotted on its adaptively binned light curve (orange crosses). For very faint bins of the fixed binning light curve we plotted only the upper limits (down-pointing green arrows).

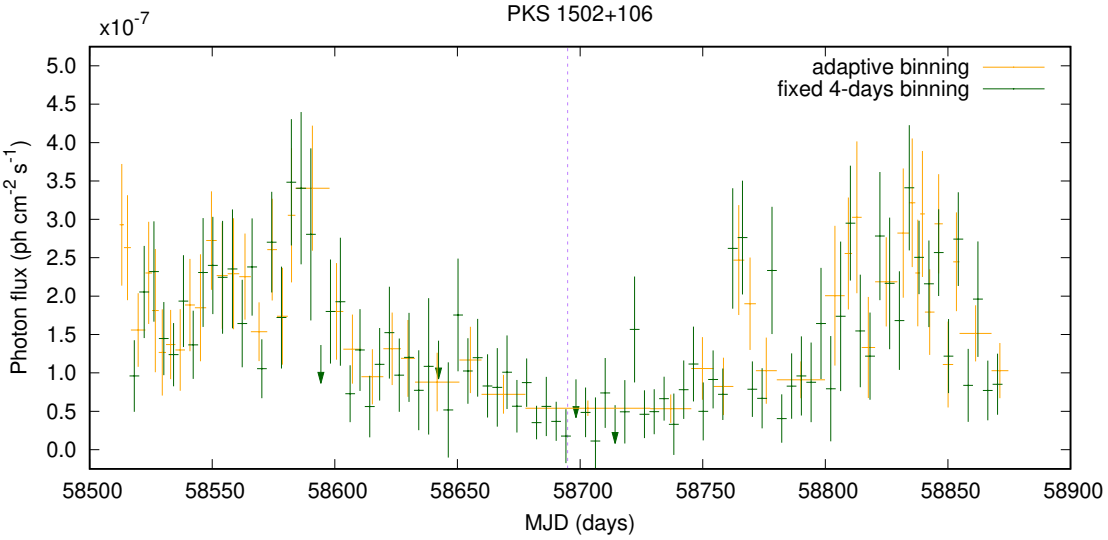

Fig. C.2. Light curve of PKS 1502+106 with fixed binning (green crosses) overplotted on its adaptively binned light curve (orange crosses). For very faint bins of the fixed binning light curve we plotted only the upper limits (down-pointing green arrows).